
Biophysical
Journal
Volume 114
Number 8
April 24, 2018
www.biophysj.org
The Premier Journal of Quantitative Biology
Biophysical Society
Published by Cell Press
for the Biophysical Society

Biophysical Journal
Article

Biophysical Society

Effect of Methylation on Local Mechanics and Hydration Structure of DNA

Xiaojing Teng[1] and Wonmuk Hwang[1,2,3,*]
[1]Department of Biomedical Engineering and [2]Department of Materials Science & Engineering, Texas A&M University, College Station, Texas; and [3]School of Computational Sciences, Korea Institute for Advanced Study, Seoul, Korea

ABSTRACT Cytosine methylation affects mechanical properties of DNA and potentially alters the hydration fingerprint for recognition by proteins. The atomistic origin for these effects is not well understood, and we address this via all-atom molecular dynamics simulations. We find that the stiffness of the methylated dinucleotide step changes marginally, whereas the neighboring steps become stiffer. Stiffening is further enhanced for consecutively methylated steps, providing a mechanistic origin for the effect of hypermethylation. Steric interactions between the added methyl groups and the nonpolar groups of the neighboring nucleotides are responsible for the stiffening in most cases. By constructing hydration maps, we found that methylation also alters the surface hydration structure in distinct ways. Its resistance to deformation may contribute to the stiffening of DNA for deformational modes lacking steric interactions. These results highlight the sequence- and deformational-mode-dependent effects of cytosine methylation.

INTRODUCTION

DNA methylation plays crucial roles in gene regulation (1–3). For vertebrates, it typically occurs on the cytosine C5 atom in the CpG (CG/CG) dinucleotide step (Fig. 1 *a*) (3,4). Cytosine (CYT) methylation leads to gene suppression (5–7), chromosome inactivation (8,9), and genomic imprinting (10,11). Abnormal hypermethylation of the CpG-rich region (CpG island) is frequently observed in cancer cells (12–14). The CpG methylation is heritable (6,15,16), further highlighting its significance in development and disease progression. The methyl group on 5-methyl-CYT (mCYT) directly affects interaction with DNA-binding proteins. For example, it blocks transcription factors (17–19) or allows binding of methyl-CpG-binding domain proteins (20–24). In addition, methylation influences nucleosome formation and stability (25–31). Though it is known to suppress nucleosome formation (26,27,29,31), opposite results have also been reported (25,28,30). Another study suggests that CpG methylation has no effect on nucleosome stability (32). These findings indicate that the effect of methylation on the conformational behavior of DNA may depend on the local sequence around the methylation site (33). A central aspect in this regard is mechanics. Flexibility significantly influences protein binding to DNA (34–37) and packing of DNA, such as in nucleosome formation (26,27,29,31,38). Although it is generally agreed that DNA becomes stiffer upon methylation (26,29,31,39–41), its dependence on local DNA sequences has not been established.

Because experiments on DNA mechanics so far do not have dinucleotide-level resolution, molecular dynamics (MD) simulations have been instrumental for gaining insight into sequence dependence (42–47). However, previous computational studies show varied results: cytosine methylation either stiffens DNA (26,31,40,48,49) or has no effect (44). It has even been proposed that flexibility increases upon methylation (50). In addition to the sequence of DNA used, these studies differ based on how flexibility is quantified. A common approach for measuring flexibility is to analyze the fluctuation in the helicoidal parameters, with lower levels of fluctuation indicating stiffer DNA (26,31,40,50). Among these studies, only (50) reports increased flexibility of the CpG step upon methylation. In (48), the overall flexibility for a given oligo was computed for comparison with the corresponding DNA cyclization experiments. The isotropic B-factor of each basepair has also been used as a measure of flexibility (49). A more detailed

Submitted December 20, 2017, and accepted for publication March 14, 2018.

*Correspondence: hwm@tamu.edu

Xiaojing Teng's present address is Department of Chemistry, Georgetown University, Washington D.C.

Editor: Antoine van Oijen.

https://doi.org/10.1016/j.bpj.2018.03.022

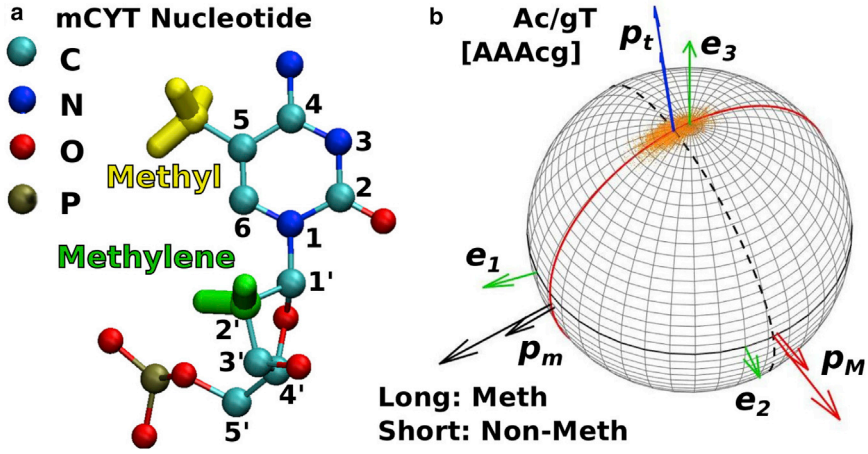

FIGURE 1 Effect of cytosine methylation on the dinucleotide step motion. (*a*) The structure of a methylated cytosine is shown. C5-methyl and C2'-methylene groups are marked by thicker bonds. Hydrogen atoms bonded to other heavy atoms are not displayed. (*b*) Conformational motion of a dinucleotide step is shown (46). An example of the Ac/gT step in [AAAcg] is given (see Fig. S1 for other steps). $\{\boldsymbol{e}_1,\boldsymbol{e}_2,\boldsymbol{e}_3\}$: the reference triad assigned to the first basepair within a dinucleotide step (d(AT) pair in this case) is shown. Orange dots: the trajectory of $\boldsymbol{e}_3'$ for the next d(cg) pair is shown. $\{\boldsymbol{p}_m,\boldsymbol{p}_M,\boldsymbol{p}_t\}$: the equilibrium triad for the next basepair in a dinucleotide step ($\boldsymbol{p}_m/\boldsymbol{p}_M$: minor/major principal axes). Long/short arrows: equilibrium triads for methylated/nonmethylated steps. The calculated values of measured quantities are in Table S1. To see this figure in color, go online.

analysis utilizing umbrella sampling with simplified helicoidal parameters suggested that the stiffness of the CG step is minimally affected by methylation (44).

The above results suggest that, although computer simulations generally agree with experimental observations regarding the flexibility of methylated DNA, the atomistic origin is not well-understood. Another important aspect of cytosine methylation is alteration of the local hydration structure. Presence of the methyl group reduces the solvation energy (40,51), which is expected given its nonpolar nature. It was further argued that this reduces the accessible conformational space and contributes to the stiffening of the methylated DNA (40). A similar explanation about the relation between solvation and stiffness was given, which considered up to the first hydration shell around the methyl group (52). However, these studies were conducted on particular DNA sequences. Furthermore, because DNA is a three-dimensional structure, analysis of its flexibility should take the direction of deformation into account. In a related vein, alteration of the hydration structure under different deformational modes has not been previously considered. A comprehensive, atomistic picture of the deformation of DNA and hydration is of broader significance because the dynamics of surface water molecules is critical for the conformational motion of biomolecules in general (53–56).

Here, we perform MD simulations to elucidate atomistic mechanisms for the methylation-induced flexibility changes in B-DNA oligos. We use a principal-axis-based orthogonal order parameter system that effectively describes DNA as an elastic rod (46). We also construct the hydration map to compare changes in surface hydration structures as methylated or nonmethylated DNA oligos undergo conformational motion. We find that methylation stiffens DNA in a sequence-dependent manner, whereas its equilibrium conformation remains similar to that of the nonmethylated DNA. Stiffening occurs for dinucleotide steps neighboring the ^{Me}CpG step (^{Me}C: mCYT). Steric interactions between the C5-methyl group of mCYT with the nonpolar groups on the 5′ side are largely responsible for the stiffening, especially the C2'methylene group of deoxyribose (Fig. 1 *a*) and the C5-methyl group of thymine (THY). Stiffening is further enhanced for consecutive ^{Me}CpG steps because the steric interactions are present on both DNA strands. This may play a role in the "methylation threshold" required to inactivate certain genes (57). However, when the base on the 5′ side of mCYT is not THY, the major bending mode does not cause any significant steric interaction. In such cases, resistance to the major bending arises from positional constraints imposed on the water molecules surrounding the mCYT-methyl group. By comparison, the major groove of the nonmethylated step is more accessible to the bulk water, and its hydration structure readily adjusts as DNA deforms. In addition to providing a coherent, atomistic picture for diverse experimental observations on DNA mechanics and hydration, the analysis presented here is likely to be useful for studying the effects of other types of covalent modifications of DNA and RNA (31,58).

METHODS

DNA oligo generation

The oligos used for simulation are listed in Table 1. Except for $[cg]_8$ and $[cg]_6$, both ends of each oligo were capped by $d(CGCG)_2$ to prevent fraying (59–61). All oligos were built in the B-DNA form by using X3DNA (62). Hydrogen atoms were added to the oligos by using CHARMM (Chemistry at Harvard Macromolecular Mechanics) (63). Four oligos, [AAAcg], [TTTcg], $[cg]_8$, and [CGcg], were used for our main analyses. The first two have a ^{Me}CpG dinucleotide step in the middle, flanked by Ac/gT and Tc/gA, respectively. We compared $[cg]_6$ with $[cg]_8$ to examine the length dependence, and [GCgc] was used to check the effect of having a single Gp^{Me}C step. The nonmethylated oligos [AAACG] and [TTTCG] were used for comparison with [AAAcg] and [TTTcg], respectively. Data for the nonmethylated CG repeat ([CGCG]) were from our previous study (46). These oligos cover most of the sequences surrounding the ^{Me}CpG step in the B-DNA form. We did not include the Cc/gG step because the

TABLE 1 Names and Sequences of DNA Oligos Used in Simulation

Name	Sequence	Steps Studied
[AAAcg]	d(CGCGAAAcgTTTCGCG) d(CGCGAAAcgTTTCGCG)	Ac/gT, cg/cg
[TTTcg]	d(CGCGTTTcgAAACGCG) d(CGCGTTTcgAAACGCG)	Tc/gA, cg/cg
$[cg]_8$	d(cgcgcgcgcgcgcgcg) d(cgcgcgcgcgcgcgcg)	cg/cg, gc/gc
[CGcg]	d(CGCGCGCGcgCGCGCG) d(CGCGCGcgCGCGCGCG)	Gc/gC, cg/cg
$[cg]_6$	d(cgcgcgcgcgcg) d(cgcgcgcgcgcg)	gc/gc
[GCgc]	d(CGCGCGCgcGCGCGCG) d(CGCGCGCgcGCGCGCG)	gc/gc
[AAACG]	d(CGCGAAACGTTTCGCG) d(CGCGAAACGTTTCGCG)	AC/GT, CG/CG
[TTTCG]	d(CGCGTTTCGAAACGCG) d(CGCGTTTCGAAACGCG)	TC/GA, CG/CG

The sequence for each strand is given in the 5′ to 3′ direction. The lower-case "c" refers to mCYT, and "g" is the complementary guanine of mCYT.

nonmethylated CC/GG step readily turns into the A-DNA form (46,64). The conformational transition of methylated DNA (49) is the subject of a separate study.

MD simulation

We used CHARMM version 40a1 (63) with the param36 all-atom force field (65) and the transferable intermolecular potential with three points (TIP3P) model (66). Each DNA oligo was solvated in a cubic water box of side length ~84 Å to make the oligo at least 15 Å away from the boundary in all directions, which is larger than the 12 Å cutoff for nonbonded interactions. Sodium ions were added at ~90 mM concentration to neutralize the system (26,67,68). The system was then subjected to the initial energy minimization (600 steps of the steepest descent method followed by 1000 steps of the adapted basis Newton-Raphson method). During energy minimization, heavy atoms of DNA were harmonically restrained with a spring constant of 2 kcal/(mol • $Å^2$). This was reduced to 1 kcal/(mol • $Å^2$) during 30 ps heating (0–300 K) and to 0.2 kcal/(mol • $Å^2$) during 70 ps equilibration runs. Heating and equilibration were done using the constant pressure (1 atm) and temperature method (69). Production runs were at 300 K under constant volume (NVT) without any restraint on DNA. They lasted 100 ns except for [GCgc] (50 ns) and [TTTCG] (150 ns). The longer time for [TTTCG] was to avoid the influence of the transient breakage of an A-T pair next to a C-G pair during 71–86 ns. As noted previously (46), using the interval during which the A-T pair remains intact gives a reasonable estimate for the stiffness of the associated dinucleotide step.

We used the SHAKE (70) algorithm to fix the length of covalent bonds for hydrogen atoms and used a 2 fs integration time step. The particle mesh Ewald summation method was used to account for long-range electrostatic interactions (71). Simulation systems typically had ~61,000 atoms, and the domain decomposition module of CHARMM was used to achieve efficient parallelization of simulation (72). Coordinates were saved every 10 ps (10^4 coordinate frames for 100 ns). Analysis of the coordinate trajectory was done for the last 50 ns (5000 frames) except for [GCgc], for which the last 25 ns was used (2500 frames). To avoid end effects, only the middle eight basepairs of oligos were used for analysis.

Calculation of helicoidal parameters, such as roll, tilt, and the helicoidal twist, was done using X3DNA (62). Molecular structures were rendered by using visual molecular dynamics (73). For figures and Supporting Material that display the hydration map, University of California at San Francisco Chimera (74) was used.

Principal axis-based analysis of DNA mechanics

The main idea of this approach is to find the most and least flexible bending directions of a dinucleotide step (principal axes) and to describe the local deformation of DNA using four order parameters: the major and the minor bending angles, twist about the direction perpendicular to the two principal axes (axial direction), and extension in the axial direction. By construction, the four order parameters form an orthogonal set for the deformation of DNA as an elastic rod, which can be directly used to estimate larger-scale quantities, such as the persistence length or the elastic energy of deformation (46).

To find the principal axes, local triads $\{\boldsymbol{e}_1, \boldsymbol{e}_2, \boldsymbol{e}_3\}$ (orthonormal coordinate bases) are first assigned to individual basepairs. The axial vector $\boldsymbol{e}_3$ is perpendicular to the best-fit plane of a basepair. $\boldsymbol{e}_1$ is perpendicular to both $\boldsymbol{e}_3$ and the vector from C8 of purine to C6 of pyrimidine, which fixes $\boldsymbol{e}_2 = \boldsymbol{e}_3 \times \boldsymbol{e}_1$. Denote the triads for the two basepairs forming a dinucleotide step as $\{\boldsymbol{e}_1, \boldsymbol{e}_2, \boldsymbol{e}_3\}$ and $\{\boldsymbol{e}_1', \boldsymbol{e}_2', \boldsymbol{e}_3'\}$, respectively. The trajectory of $\boldsymbol{e}_3'$ relative to $\{\boldsymbol{e}_1, \boldsymbol{e}_2, \boldsymbol{e}_3\}$ forms an ellipsoidal set of dots (*orange dots* in Figs. 1 *b* and S1). Its centroid vector $\boldsymbol{p}_t$ corresponds to the equilibrium-bending direction of the dinucleotide step. The long and short axes of the ellipsoid form the major and minor bending directions (*red solid* and *black dashed circles* in Figs. 1 *b* and S1). The axes perpendicular to these directions are, respectively, the major and the minor principal axes of bending, $\boldsymbol{p}_M$ and $\boldsymbol{p}_m$. The set $\{\boldsymbol{p}_m, \boldsymbol{p}_M, \boldsymbol{p}_t\}$ forms a right-handed orthonormal system that we call the equilibrium triad. The orientation of the equilibrium triad relative to $\{\boldsymbol{e}_1, \boldsymbol{e}_2, \boldsymbol{e}_3\}$ represents the equilibrium conformation of a given dinucleotide step.

The major/minor bending angle of a step at each time frame can be measured as the projection angles of $\boldsymbol{e}_3'$ onto the major and minor directions (*circles* in Figs. 1 *b* and S1). The reference direction for the bending angle measurement is $\boldsymbol{p}_t$, so a zero bending angle means that the dinucleotide step takes the equilibrium curvature. The twist angle of a step at each frame was obtained by measuring the Euler angle between the current triad $\{\boldsymbol{e}_1', \boldsymbol{e}_2', \boldsymbol{e}_3'\}$ and the equilibrium triad $\{\boldsymbol{p}_m, \boldsymbol{p}_M, \boldsymbol{p}_t\}$ about $\boldsymbol{p}_t$. The extension of a dinucleotide step was calculated from the distance between the centroids of neighboring triads (the centroid for a triad is at the midpoint between C8 of purine and C6 of pyrimidine for the corresponding basepair). The stiffness of each deformational mode was calculated by applying the equipartition theorem, which is inversely proportional to the variance of the order parameter (46,75). C++ and MATLAB (The MathWorks, Natick, MA) codes for calculating the equilibrium triads and the stiffnesses of the four order parameters from simulation trajectories are provided in Data S1.

Water density map

We constructed the water density map (hydration map) based on our previously developed approach (76). Briefly, the space within 20 Å from a given set of reference atoms (region of interest) was divided into cubic cells of linear size 0.7 Å (half the approximate radius of a water molecule). The fraction of coordinate frames during which a water oxygen atom visits a cell divided by the cell volume (0.7^3 $Å^3$) yields the local water density. As the oligo moves in space, the cells also move with the reference atoms. If the reference atoms undergo large conformational motion, the locations of cells relative to them become less defined. We thus used a dinucleotide step for reference instead of using the entire oligo. For visualization, maps were saved in the Medical Research Council electron-density file format. The method for calculating the hydration map for a given simulation trajectory has been incorporated into CHARMM.

To construct the hydration map under large deformations of DNA (Figs. 7 and 8), coordinate frames from the last 50 ns, during which one of the order parameters is higher or lower than the average by one SD, were used. In these subsets of coordinate frames, distributions of the other order parameters are minimally affected because they are orthogonal. The structure for

the orientational reference was taken from a coordinate frame in which the corresponding order parameter is close to the average value for the selected frames with large deformations.

RESULTS AND DISCUSSION

Effect of methylation on conformational properties of dinucleotide steps

We quantified the conformational motion of a dinucleotide step by assigning triads to each basepair and analyzing their relative motion. For all dinucleotide steps, the equilibrium triad $\{\boldsymbol{p}_m, \boldsymbol{p}_M, \boldsymbol{p}_t\}$ changes its orientation very little upon methylation, suggesting that the equilibrium curvature of DNA is largely unaffected (Figs. 1 *b* and S1). This is consistent with previous simulations that yielded no significant changes in the average values of helicoidal parameters of certain methylated DNA oligos (31,40). Similar to the nonmethylated case (46), distributions of the major and minor bending angles for the methylated cases closely follow Gaussian, indicating that their bending motion can be described by linear elasticity (Figs. 2 and S2). Distributions of twist angles are more strongly affected (e.g., Fig. 2, *c* and *f*). Because twist measures the rotation of $\{\boldsymbol{e}_1', \boldsymbol{e}_2', \boldsymbol{e}_3'\}$ about $\boldsymbol{p}_t$, it is decoupled from the orientation of the equilibrium triad; hence, it does not have any major impact on the local contour of DNA (77).

We calculated the stiffness associated with major/minor bending and twist and compared values between methylated and nonmethylated cases (Fig. 3; values are in Table S2). Dinucleotide steps away from the methylation site have stiffnesses that are overall similar to those of nonmethylated oligos (marked "B.N." in Fig. 3, *a*, *b*, and *d*). For the ^{Me}CpG step, stiffness does not change significantly upon methylation (*star* in Fig. 3). This agrees with a previous one-dimensional umbrella sampling simulation of the ^{Me}CpG step, showing that its flexibility is unaffected by methylation (44). A more prominent increase in stiffness was observed for steps neighboring the ^{Me}CpG step (marked "N" in Fig. 3). The major and minor bending stiffnesses increase from 17% ([TTTcg]) to 36% ($[cg]_8$) and from 33% ([AAAcg]) to 74% ($[cg]_8$), respectively. The twist stiffness also increases from 20% ([CGcg]) to 67% ($[cg]_8$). A similar trend was observed for the extensional stiffness κ_E (Fig. S3).

Thus, methylation stiffens the neighboring steps rather than the methylated step itself. It is also worth noting that

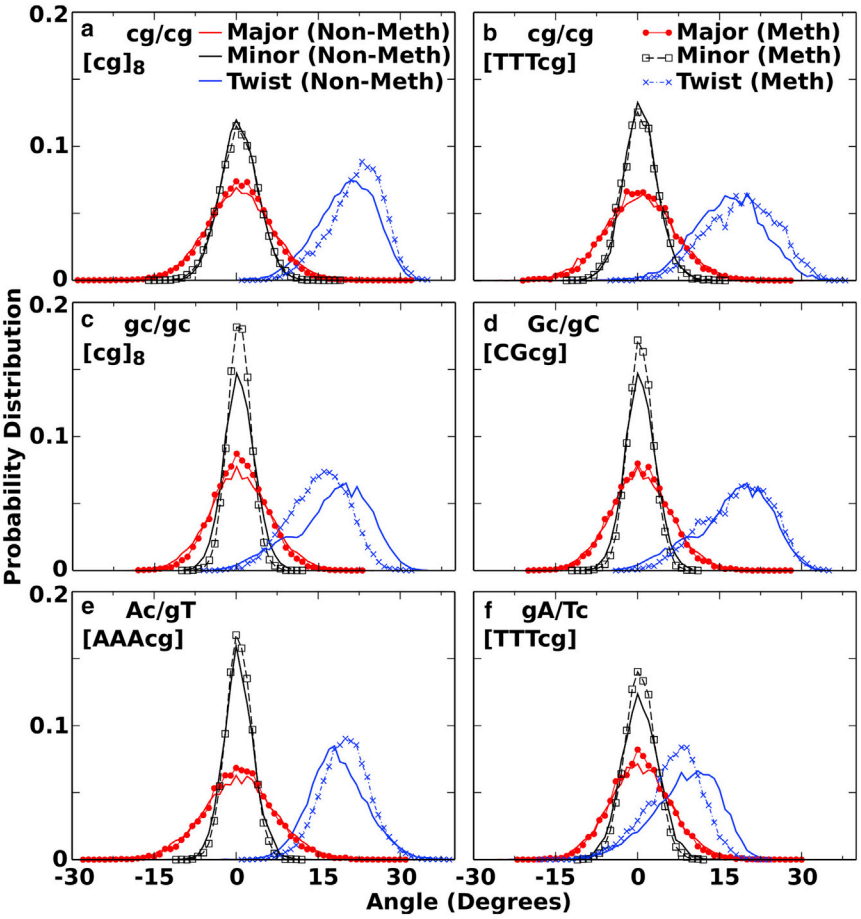

FIGURE 2 (*a–f*) Distributions of angles with and without methylation (*lines* with and without symbols, respectively). The names of the dinucleotide step and the oligo used for the analysis are shown in each panel. References for the major and minor bending angles (along the *red solid* and *black dashed circles* in Figs. 1 *b* and S1) are the equilibrium direction $\boldsymbol{p}_t$, so that their distributions are peaked at zero degrees. Fig. S2 plots distributions for the major and minor bending angles on logarithmic scales, which reveals their Gaussian nature more clearly. To see this figure in color, go online.

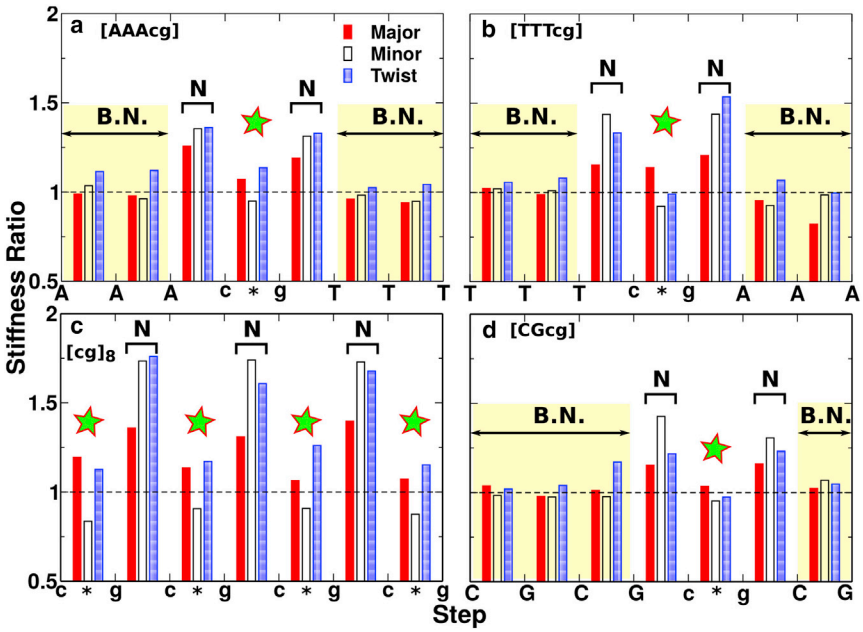

FIGURE 3 (*a–d*) Ratio of dinucleotide stiffness between methylated and nonmethylated oligos. Star, ^{Me}CpG step. "N," neighboring steps. "B.N.," region beyond neighbors. A similar plot for the extensional stiffness is in Fig. S3. To see this figure in color, go online.

as the density of methylation increases (Fig. 3, *c* and *d*; $[cg]_8$ vs. [CGcg]), stiffening is further enhanced. This indicates that hypermethylation of the CpG island alters the mechanical property of DNA more than linear superposition of individual methylated steps, which may be related to the "methylation threshold" requirement for inactivating certain genes (57). Its structural origin is explained below.

Among the helicoidal parameters, roll, tilt, and the helicoidal twist approximately correspond to the two directions of bending and the twist in our principal axis-based system. For comparison, we used fluctuations of these three helicoidal parameters to calculate their apparent stiffnesses, which show a similar trend to that for the principal axis-based stiffness (Fig. S4). This is expected because stiffening of neighboring steps will also reduce fluctuations in helicoidal parameters. However, the changes are not as pronounced as the results of our principal axis-based analysis, and the helicoidal stiffness of the ^{Me}CpG step itself also increases in some cases. This is due to the difference between our motion-based orthogonal order parameters and the atomic-structure-based helicoidal parameters, where the former more clearly describe the deformational modes of DNA.

Structural basis for the altered stiffness

The changes in stiffness can be explained mainly in terms of the interactions between the mCYT-methyl group and other nonpolar groups of the neighboring nucleotide (Figs. 1 *a* and 4 *a*). Because of the right-handed structure of B-DNA, the nucleotide on the 5′ side of ^{Me}CpG is closer to the mCYT-methyl group than that on the 3′ side. Steric interaction with nearby groups upon large deformation can suppress conformational fluctuation of the step, thereby increasing the stiffness of neighboring steps (Fig. 4). Within the ^{Me}CpG step itself, the methyl groups do not interact, and hence, its stiffness is similar to that of the nonmethylated case.

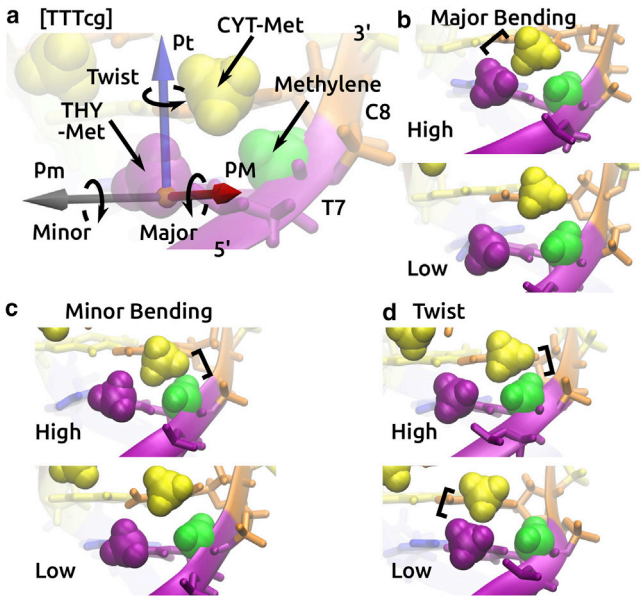

FIGURE 4 Steric interaction between the mCYT-methyl and adjacent nonpolar groups. (*a*) [TTTcg] is used for illustration. Yellow, mCYT-methyl. Green, C2'-methylene (present in all nucleotides; Fig. 1 *a*). Purple, THY-methyl group. Circular arrows, directions of rotation where major/minor bending and twist angles increase. (*b–d*) Examples show where high or low values of angles cause steric contact with the mCYT-methyl group (marked by *square bracket*). (*b*) shows major bending. (*c*) shows minor bending. (*d*) shows twist. The structures in each panel have the angle in question taking high or low values, whereas the other two angles are close to their averages. To see this figure in color, go online.

For the neighboring steps, steric interactions depend on the type and the direction of deformation. High major/minor bending leads to a clash of the mCYT-methyl group with the THY-methyl/C2'-methylene groups, respectively (Fig. 4, *b* and *c*). Low major or low minor bending do not incur any noticeable clash. On the other hand, high/low twist leads to a clash with C2'-methylene/THY-methyl groups, respectively (Fig. 4 *d*). If the base on the 5′ side of mCYT is not THY, the interaction with the THY-methyl group is absent. This is supported by the overall greater increase in stiffness of the neighboring steps in [TTTcg] compared to those in [AAAcg] and [CGcg] (Figs. 3 and S3). Yet, $[cg]_8$, which has consecutive ^{Me}CpG steps, exhibits the greatest increase in stiffness of the neighboring steps. To test whether this effect depends on the length of oligos, we used $[cg]_6$, which contains fewer ^{Me}CpG steps. However, its stiffness is nearly the same as that for $[cg]_8$ (Fig. S5 *a*). We found that the stiffness enhancement is a more local effect; the two mCYTs within a gc/gc step (sandwiched between two ^{Me}CpG steps) interact with C2'-methylene groups on both DNA strands (Fig. S5 *b*). To further test this, we used [GCgc], which contains a Gp^{Me}C step (physiologically less relevant (3,4)). Despite having only a single Gp^{Me}C step, its stiffness is similar to that of $[cg]_8$ (Fig. S5 *a*). This confirms that the stiffness enhancement is due to the doubling of the interaction between mCYT-methyl and C2'-methylene.

To quantitatively analyze the interaction, we measured two-dimensional (2D) histograms of the minimal distance for the mCYT-methyl and C2'-methylene pair versus the four order parameters (Fig. 5, *a–d*). For [TTTcg], the mCYT-methyl and THY-methyl minimal distance histogram was measured as well (Fig. 5 *e*). For the major bending, 2D histograms of the mCYT-methyl and C2'-methylene pair do not show any significant asymmetry, suggesting that the interaction is not strong in this mode (Fig. 5, *a–d*, column 1). For mCYT-methyl and THY-methyl, the histogram is skewed to low major bending angle (Fig. 5 *e*, column 1), which agrees with the increasing steric interaction at higher major bending angle (Fig. 4 *b*). 2D histograms for the minor bending also show trends that are consistent with the steric interactions illustrated in Fig. 4 *c*; for mCYT-methyl and C2'-methylene, the histograms are tilted to low minor bending angles because high minor bending leads to steric clash (Fig. 5, *a–d*, column 2), whereas no such bias is present for mCYT-methyl and THY-methyl (Fig. 5 *e*, column 2). For twist, the 2D histograms involving the C2'-methylene and THY-methyl groups tilt in opposite directions (Fig. 5, column 3), which is also in agreement with our structural analysis (Fig. 4 *d*). In the case of extension, 2D histograms for C2'-methylene are skewed to larger values, whereas the histogram is symmetric for THY-methyl (Fig. 5, column 4), which suggests that the former contact becomes significant at low extensions.

We further generated 2D histograms of the interaction energy (electrostatic and Lennard-Jones) between the groups mentioned above. They have skewing directions approximately opposite to those of the minimal distance histograms (Fig. 5 versus Fig. S6). This is because high-energy states are visited less. However, the trend is not as clear because interactions between atoms that are not in close contact also contribute to the measured energy. In a related vein, because the neighboring atoms are in near-contact in equilibrium, the effect of steric interaction gradually increases with angles rather than being limited only to large angles (Fig. S2).

As another means of probing asymmetric deformation (compared to nonmethylated cases), we recalculated the distributions of angles for the steps in the methylated oligos using the corresponding equilibrium triads in nonmethylated oligos (Fig. S7). The distributions for the methylated cases (Figs. 2 and S2) do not exhibit noticeable asymmetry because the equilibrium triads are constructed based on centers of respective distributions (cf. Fig. 1 *b*). In comparison, the distributions of methylated cases based on the equilibrium triads of the nonmethylated cases, though approximate, do reveal the tendency for higher angles to be suppressed for the steps neighboring the ^{Me}CpG step (Fig. S7, *c–f*).

The dependence of steric interactions on the deformational mode is consistent with the enhancement of the minor bending and twist stiffness of neighboring steps (Fig. 3). Because the mCYT-methyl and C2'-methylene interactions are present in all neighbor steps, the minor bending stiffness increases to a similar extent across all oligos, and for $[cg]_8$, it further increases because of the doubling of this interaction (Fig. S5). The large increase in the twist stiffness of [TTTcg] (Fig. 3 *b*) may be attributed to the additional interaction involving the THY-methyl group for low twist (Fig. 4 *d*). On the other hand, the increase in the major bending stiffness does not correlate well with this steric mechanism. Despite the interaction between mCYT-methyl and THY-methyl upon high major bending (Fig. 4 *b*), the increase in the major bending stiffness of [TTTcg] is not particularly high compared to that of other oligos (Fig. 3 *b*). Additional factors must affect the major bending of the other oligos, for which we found that surface hydration may play a significant role.

Organization of surface water

In addition to directly affecting intra-DNA interactions, cytosine methylation alters the organization of nearby water molecules. Adopting our previously developed method (76), we calculated the water density map, which yields the probability density of a water oxygen at a given location relative to DNA in 0.7 Å resolution. The calculated map was visualized with a certain density cutoff. With a cutoff equal to the bulk water density (0.0333 $Å^{-3}$), the hydration map takes a round morphology consisting of two protruding rims following the double-helical phosphate backbone (*red part* in Fig. 6 *a*). Water molecules that are

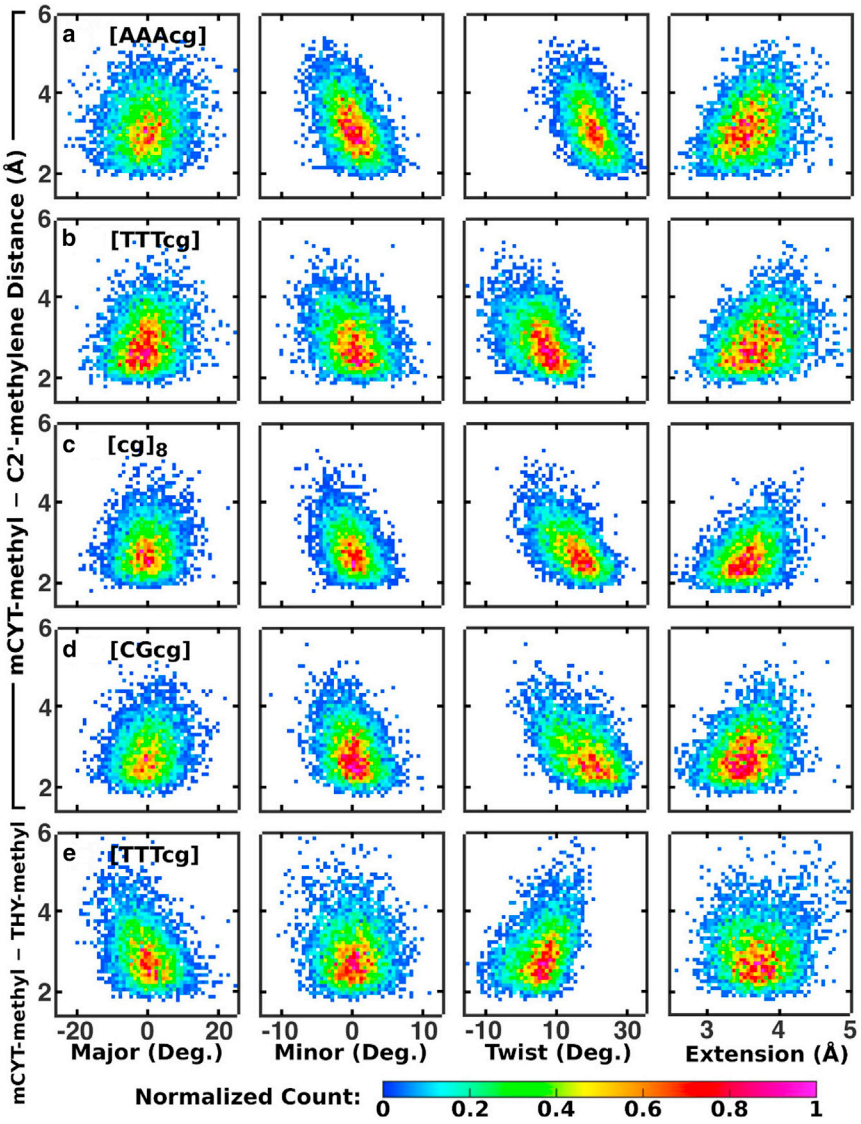

FIGURE 5 2D histograms of order parameters versus the minimal distance between the mCYT-methyl group, with (*a*)–(*d*) the neighboring C2'-methylene and (*e*) the THY-methyl group in [TTTcg] on the 5′ side (cf. Fig. 4). To see this figure in color, go online.

further away from DNA than this move without any defined positional relation relative to DNA, so that they have low and diffuse density profiles. Thus, the region displayed with the bulk density cutoff defines an approximate range in which water molecules move together with DNA. Its boundary is at ∼15 Å from DNA's axis, defining the radius of a hydrated DNA. Considering the 10 Å atomic radius of DNA and the 2.8 Å distance between water molecules, the hydrated DNA contains two hydration shells from the phosphate backbone, which agrees with previous findings (78–80). At this level, the density maps look similar across all oligos.

More specific hydration structure is revealed at higher density cutoffs. We first used 1.5 times the bulk water density (0.05 $Å^{-3}$; Videos S1, S2, S3, S4, S5, S6, and S7). Viewed along the major groove of the oligo, the second hydration shell is no longer present, and the "herringbone" structure of the first hydration shell around phosphate groups is visible along the double-helix backbone (Fig. 6 *b*; Videos S1, S2, S3, S4, S5, S6, and S7).

Differences in hydration structure between methylated and nonmethylated cytosines can be seen in the major groove. With a cutoff at 1.5 times the bulk density, each mCYT-methyl group is surrounded by an onion-like hemispherical hydration shell (Fig. 6 *b*), which is reminiscent of the clathrate structure around nonpolar groups (81). Because of the proximity between the two methyl groups, the shells merge in the middle, forming a vertically elongated density. Similar features are found for the ^{Me}CpG steps in other oligos (Videos S1, S3, and S4). For [TTTcg], the THY-methyl groups above and below cause the central water density to shrink (Video S2). By contrast, for nonmethylated oligos, the major groove is extensively filled with stripe-like water densities (Videos S5, S6, and S7). The appearance of connected stripes instead of punctate blobs indicates that a certain degree of positional flexibility is

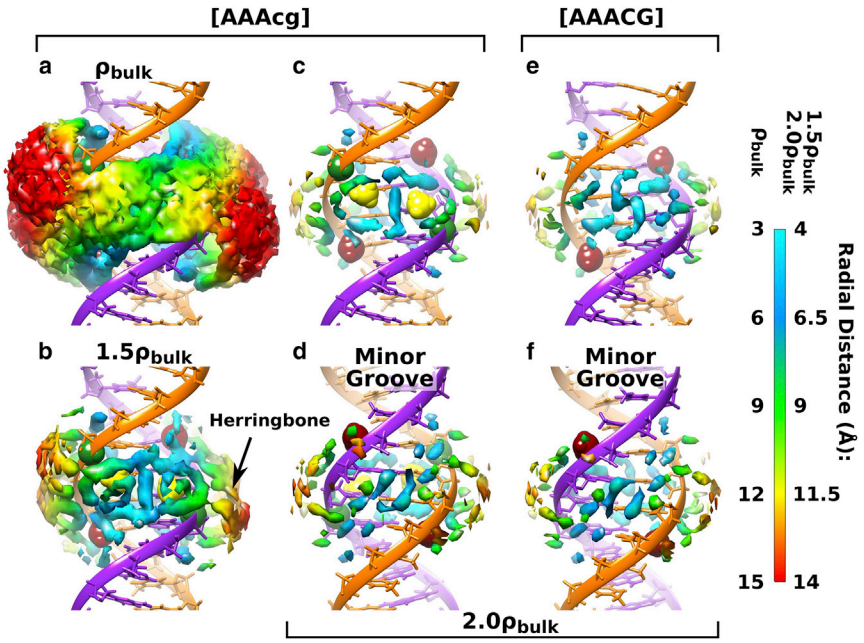

FIGURE 6 Water density map around the central dinucleotide step of (*a–d*) [AAAcg] and (*e* and *f*) [AAACG]. The viewing direction is (*a*)–(*c*) and (*e*) the major groove, and (*d*) and (*f*) the minor groove. The water density cutoffs used were as follows: (*a*) bulk value (ρ_{bulk}), (*b*) 1.5 times, and (*c–f*) two times the bulk value. The color scale shows the distance from the DNA's axis. mCYT-methyl (*yellow*), THY-methyl (*dark red*), and C2'-methylene on the 5′ side of the ^{Me}CpG step (*green*) are rendered as spheres (cf. Fig. 4 *a*). Videos S1, S2, S3, S4, S5, S6, S7, S8, S9, S10, S11, S12, S13, and S14 display density maps of different oligos with cutoffs at 1.5 times (Videos S1, S2, S3, S4, S5, S6, and S7) and 2.0 times (Videos S8, S9, S10, S11, S12, S13 and S14) the bulk density. Overlaid views of maps in (*c*) and (*e*) and similar views for other oligos are in Fig. S8. To see this figure in color, go online.

present for water molecules that form hydrogen bonds with the major groove of DNA.

Using a cutoff at twice the bulk water density reveals more clearly the locations of water molecules hydrogen-bonded to DNA (Figs. 6, *c* and *e* and S8; Videos S8, S9, S10, S11, S12, S13, and S14). The outer side of the hydration shell covering the mCYT-methyl group is not visible, as its density is lower than the cutoff used. The remaining hydration shell forms a characteristic "double-D ring" around the two mCYT-methyl groups (Fig. 6 *b* versus *c*; also see Videos S8, S9, S10, S11, S12, S13, and S14). For the non-methylated oligos, the stripe-like densities break and have a reduced volume. Without the methyl groups that impose constraints on the arrangement of water molecules, water density does not organize into any particular patterns such as the double-D ring. Instead, their locations more closely follow hydrogen bonding to the major groove and the phosphate backbone atoms.

The hydration map in the minor groove depends less on methylation (Fig. 6, *d* and *f*; Videos S8 and S13). In all oligos, there are two rows of densities running in parallel along the minor groove. Their elongated morphology indicates that water molecules are mobile mostly along the direction of the groove. The density profile agrees with the analysis based on crystal structures in which water molecules form "spines" along the minor groove (82). Interspersed along the spine are additional densities located radially further away from DNA's axis (*green blobs* in Fig. 6, *d* and *f*). They correspond to water molecules bridging between the spine water and the water network around the phosphate backbone. The presence of an extensive network of water molecules around DNA is consistent with a previous neutron-diffraction experiment (83).

To gain an averaged view of hydration, we calculated the radial distribution function (RDF) of water oxygen about the carbon atom in the mCYT-methyl group (C5m; Fig. 1 *a*) or about the corresponding H5 atom in the nonmethylated CYT (Fig. S9). Compared to the H5 atom, peaks for the first hydration shell of the RDF are located 0.8–0.9 Å away from the C5m atom because of the larger size of the mCYT-methyl group. The density of the peak is also higher in the methylated case (Fig. S9) because the hydration shell forms a ring around the methyl groups, whereas it is more punctate in the nonmethylated case (Fig. 6). In both cases, beyond ~15 Å, the RDF gradually approaches the bulk value without oscillation. This is again consistent with our hydration map analysis, revealing the extent of the solvation shell moving with DNA (Fig. 6 *a*).

We also calculated the density for Na^+. Although transient binding of ions may play a structural role (84,85), our simulation systems contain only moderate ~90 mM monovalent Na^+. Indeed, we had to lower the density cutoff for Na^+ to 0.2 times the bulk water density to visualize. It is found mainly along the center of the minor groove, and it is largely absent in the major groove (Fig. S10). This indicates that Na^+ is highly mobile and does not bind strongly to the major groove. Furthermore, because it populates mostly the minor groove, Na^+ should have little methylation-dependent effect.

Contribution of surface hydration to DNA mechanics

To find the response of water to the deformation of DNA, we constructed the hydration map based on coordinate frames in which the dinucleotide step in question exhibits a large

deformation in one of its order parameters (see Methods). We first consider deformations of the central ^{Me}CpG (cg/cg) and CG/CG steps (Fig. 7; Fig. S11; the response of water in other oligos shows similar behaviors). For high major bending, the water density in the major groove between the two mCYT-methyl groups changes from a vertically elongated shape to a round or slightly horizontal shape, as the vertical spacing in the major groove decreases. Conversely, for low major bending, the density between the mCYT-methyl groups elongates vertically (*ovals* in Fig. 7, *a* and *b*). Other parts of the double-D density ring around the mCYT-methyl groups also exhibit vertical alignment/splitting under high/low major bending (*horizontal lines* in Fig. 7, *a* and *b*). Similar responses are seen for the minor bending to a lesser extent, as the step bends the least in the minor principal direction (Fig. 7, *c* and *d*). For twist, the density between the mCYT-methyl groups becomes vertically elongated under high twist, and under low twist, it becomes horizontally wider (Fig. 7, *e* and *f*). We did not consider changes under extension because this is the stiffest deformational mode (46). In the minor groove, the water spine is more stably bound (55) so that its response to deformations of DNA is not very extensive (data not shown). Furthermore, because the hydration in the minor groove does not depend on methylation (Fig. 6), we do not consider it further.

The hydration map in the major groove of the nonmethylated CG/CG step also undergoes changes as DNA deforms. High major bending or high twist reduces the size of the major groove (Fig. 4 *a*), so that the water densities become closer or merge. Converse effects occur when large deformations occur in opposite directions. Minor bending has less influence on the hydration map because it is the least bendable direction and also because DNA grooves deform laterally (Fig. 4 *a*) without much difference in size. Overall, these results show that the hydration around the ^{Me}CpG and CG/CG steps readily adapts as DNA deforms.

Next, we constructed hydration maps under large deformations of the steps neighboring the ^{Me}CpG step and the corresponding steps of the nonmethylated oligos. We focused only on the major bending of [AAAcg] and [CGcg] because their stiffnesses increase without any noticeable steric interaction (Fig. 4). In this case, water molecules in the horizontal part of the double-D ring form hydrogen bonds with the C6-carbonyl and N7 of the guanine base shared between ^{Me}CpG and its neighboring step (g9 in Fig. 8 *a* and g8 in Fig. 8 *c*). The corner-like geometry created by guanine and the mCYT-methyl group above stabilizes the horizontal parts of the double-D ring, which is maintained but displaced downward under high major bending (*horizontal lines* in Fig. 8, *a* and *c*). For the nonmethylated [AAACG], the density exists separately for the dinucleotide step, as water molecules can form hydrogen bonds with respective bases (two *horizontal lines* in Fig. 8 *b*). For [CGCG], a single horizontal density is observed, but it is thicker and is positioned halfway between G8 and C9 without any downward displacement (Fig. 8 *d*).

These results suggest that a single row of water density forming the horizontal part of the double-D ring has to satisfy the constraint that it forms hydrogen bonds with

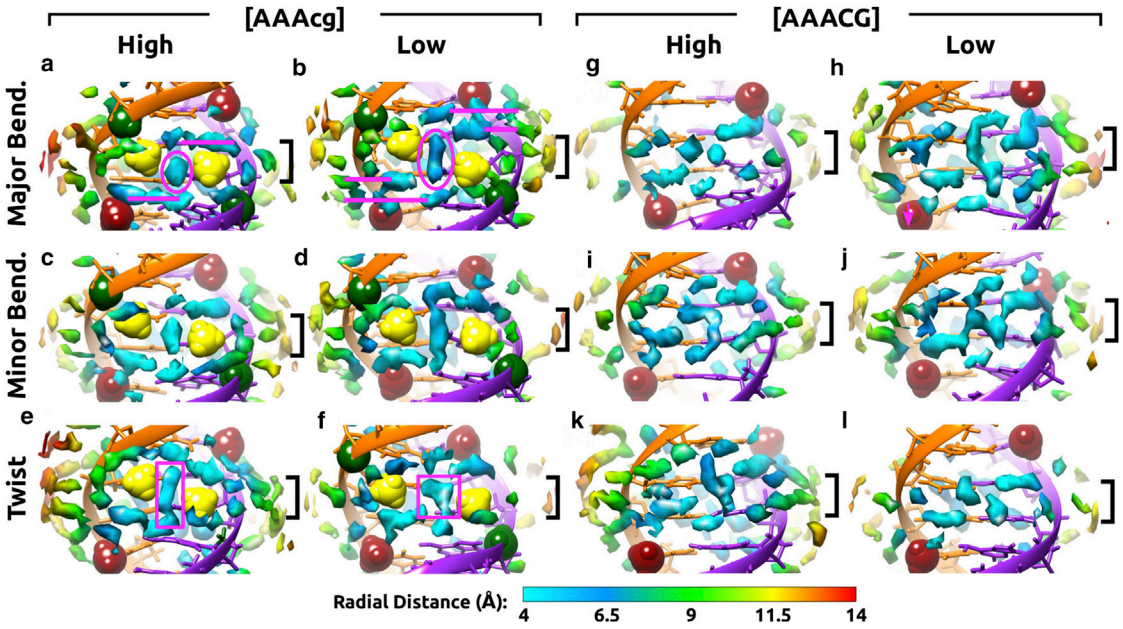

FIGURE 7 Hydration maps (cutoff at twice the bulk density) around the major grooves for large deformations of (*a–f*) ^{Me}CpG of [AAAcg] and (*g–l*) CG/CG of [AAACG] (marked by *square brackets*). Labels on the far left show deformational modes. "High" and "low" designations on top show cases in which the respective angles are higher or lower than the average by more than one SD. (*a* and *b*) Horizontal lines and ovals and (*e* and *f*) rectangles colored in pink are visual guides to highlight deformations of the hydration map. Overlaid views of these maps are in Fig. S11. To see this figure in color, go online.

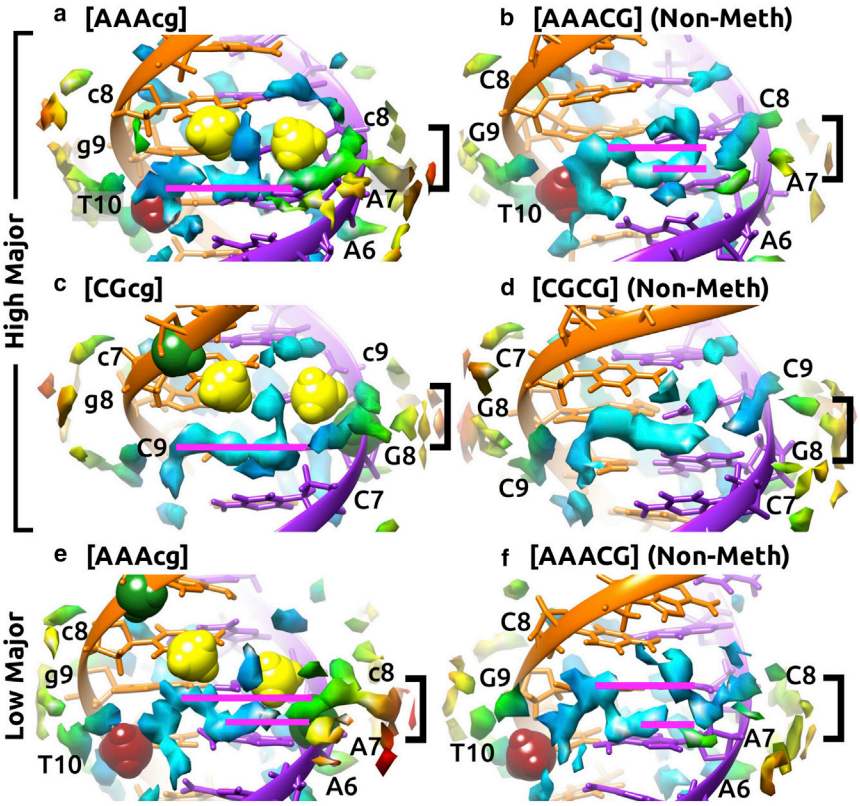

FIGURE 8 Response of hydration to large major bending of the steps neighboring (*a*, *c*, and *e*) methylated and (*b*, *d*, and *f*) nonmethylated steps (marked by *angular brackets*). (*a–d*) High major bending and (*e* and *f*) low major bending are shown. Horizontal lines are visual guides to highlight the response of water to deformation. In (*a*) and (*c*), a single row of water density is displaced downward. To see this figure in color, go online.

the neighboring base simultaneously as it is stabilized by the corner-like geometry created by the mCYT-methyl group. Because it will be more difficult to maintain hydrogen bonds with the neighboring base when the mCYT-methyl group displaces water, high major bending will be suppressed. Under low major bending, the major groove becomes more open so that the hydration can adapt more easily and form densities separately for the two basepairs in both methylated and nonmethylated cases (Fig. 8, *e* and *f*).

Circumstantial evidence for the role of hydration is found in the flexibility of DNA containing 5-hydroxymethyl cytosine, which replaces a hydrogen atom in the mCYT-methyl group with a hydroxyl group. Despite the relatively minor substitution, the stiffness of the oligo decreases (31). Because steric interaction is unlikely to be affected greatly, the drastic changes in stiffness are likely due to altered organization of water around the hydroxymethyl group. The potential role of hydration affecting the flexibility of methylated or hydroxymethylated DNA has been previously suggested for an isolated ^{Me}CG pair (52), whereas the ^{Me}CpG methylation pattern is found in mammals.

CONCLUSIONS

This study elucidates the atomistic mechanisms of the sequence- and deformational-mode-dependent stiffening of methylated DNA. Decomposing the DNA motion using the orthogonal order parameters made it possible to analyze the effects of steric interactions and the surface hydration in a direction-dependent manner. As demonstrated through different oligos (Fig. 3), stiffness is determined mainly at the dinucleotide level, where nonlocal effects by basepairs beyond immediate neighbors play secondary roles. This allows for the building of an approximate "flexibility map" for oligos with arbitrary sequences using the dinucleotide-level information (Table S2) (46).

In comparison to the steric mechanism, the role of hydration for the conformational dynamics of DNA is more difficult to assess; for this reason, we perform a qualitative analysis based on the response of the surface hydration to different deformational modes of DNA. For further testing the role of water, it should be noted that A-DNA is preferred over the B-DNA conformation at low water content (85) so that one cannot simply compare simulations with and without water. We have also calculated the interaction energies of surface water molecules hydrogen-bonded to DNA, but their large fluctuation made it difficult to draw any clear correlation with the deformation of DNA. We leave a more quantitative evaluation of the energetic contribution of water to the calculated stiffness of DNA to future studies.

Recently, other force fields for DNA have been developed, including the additive Assisted Model Building with Energy Refinement (AMBER) bsc1 and OL15 (86) and the polarizable CHARMM Drude 2017 force field (87,88). Compared to the CHARMM param36 force field used in

this study, their improvements are mostly in quantitative details in terms of deviations from experimental structures, and in the case of the Drude force field, differences in the potential energy functions of internal angles become apparent mainly for large deformations away from minima (87). Drude 2017 will thus be more suitable for studying conformational transitions and sensitive dependence on ions (88). But all of these force fields work reasonably well for equilibrium thermal fluctuations, though specific values of measured stiffness may vary to some extent. Similarly, because of the given geometry of water, its organization near DNA is expected to be similar across different force fields. Thus, our main conclusions regarding the steric- and hydration-based mechanisms should hold.

It is of interest to discuss the potential role of cytosine methylation on the flexibility of short oligos. Single-molecule experiments have shown that oligos with lengths smaller than 100 bp are more flexible compared to predictions from worm-like chain models (89–91). Models such as kinkable worm-like chains (91) and asymmetric elastic rods (92) introduce a second energy minimum at large bending angles. However, our simulations probing equilibrium thermal fluctuation did not find any bimodal behavior (Fig. 2), which is similar to the absence of bimodality in nonmethylated oligos (46,88). Furthermore, because cytosine methylation only marginally affects the equilibrium triad, it is unlikely to induce any significant changes in the curvature of DNA, which has previously been suggested to contribute to high flexibility of short nonmethylated oligos (90). Yet, our results do not preclude conformational transitions at larger deformations that were not sampled in this study.

Our study provides a base knowledge for understanding the effect of cytosine methylation on the dynamics of DNA packaging at larger scales. Another important implication of this study is that the nonpolar methyl group actively organizes and stabilizes the surrounding hydration structure. The role of hydration around nonpolar groups for the conformational dynamics of biomolecules is a problem of broad interest that warrants deeper investigation.

SUPPORTING MATERIAL

Eleven figures, two tables, fourteen videos, and one data file are available at http://www.biophysj.org/biophysj/supplemental/S0006-3495(18)30389-8.

AUTHOR CONTRIBUTIONS

X.T. and W.H. designed the research. X.T. performed the research. X.T. and W.H. developed the analytic tools. X.T. analyzed the data. X.T. and W.H. wrote the manuscript.

ACKNOWLEDGMENTS

We acknowledge the Texas A&M Supercomputing Facility (http://sc.tamu.edu) and Texas Advanced Computing Center at The University of Texas at Austin for providing computing resources. Funding for the publication of this article was supported by the Texas A&M Strategic Transformative Research Program.

REFERENCES

1. Bird, A. P. 1986. CpG-rich islands and the function of DNA methylation. *Nature.* 321:209–213.
2. Jones, P. A., and D. Takai. 2001. The role of DNA methylation in mammalian epigenetics. *Science.* 293:1068–1070.
3. Schübeler, D. 2015. Function and information content of DNA methylation. *Nature.* 517:321–326.
4. Hare, J. T., and J. H. Taylor. 1985. One role for DNA methylation in vertebrate cells is strand discrimination in mismatch repair. *Proc. Natl. Acad. Sci. USA.* 82:7350–7354.
5. Razin, A., and A. D. Riggs. 1980. DNA methylation and gene function. *Science.* 210:604–610.
6. Bird, A. 2002. DNA methylation patterns and epigenetic memory. *Genes Dev.* 16:6–21.
7. Maunakea, A. K., R. P. Nagarajan, …, J. F. Costello. 2010. Conserved role of intragenic DNA methylation in regulating alternative promoters. *Nature.* 466:253–257.
8. Panning, B., and R. Jaenisch. 1998. RNA and the epigenetic regulation of X chromosome inactivation. *Cell.* 93:305–308.
9. Takai, D., and P. A. Jones. 2002. Comprehensive analysis of CpG islands in human chromosomes 21 and 22. *Proc. Natl. Acad. Sci. USA.* 99:3740–3745.
10. Li, E., C. Beard, and R. Jaenisch. 1993. Role for DNA methylation in genomic imprinting. *Nature.* 366:362–365.
11. Jones, P. A. 2012. Functions of DNA methylation: islands, start sites, gene bodies and beyond. *Nat. Rev. Genet.* 13:484–492.
12. Jones, P. A., and S. B. Baylin. 2002. The fundamental role of epigenetic events in cancer. *Nat. Rev. Genet.* 3:415–428.
13. Esteller, M. 2008. Epigenetics in cancer. *N. Engl. J. Med.* 358:1148–1159.
14. Bergman, Y., and H. Cedar. 2013. DNA methylation dynamics in health and disease. *Nat. Struct. Mol. Biol.* 20:274–281.
15. Stein, R., Y. Gruenbaum, …, H. Cedar. 1982. Clonal inheritance of the pattern of DNA methylation in mouse cells. *Proc. Natl. Acad. Sci. USA.* 79:61–65.
16. Du, Q., Z. Wang, and V. L. Schramm. 2016. Human DNMT1 transition state structure. *Proc. Natl. Acad. Sci. USA.* 113:2916–2921.
17. Weih, F., D. Nitsch, …, P. B. Becker. 1991. Analysis of CpG methylation and genomic footprinting at the tyrosine aminotransferase gene: DNA methylation alone is not sufficient to prevent protein binding in vivo. *EMBO J.* 10:2559–2567.
18. Tate, P. H., and A. P. Bird. 1993. Effects of DNA methylation on DNA-binding proteins and gene expression. *Curr. Opin. Genet. Dev.* 3:226–231.
19. Hu, S., J. Wan, …, H. Zhu. 2013. DNA methylation presents distinct binding sites for human transcription factors. *eLife.* 2:e00726.
20. Boyes, J., and A. Bird. 1991. DNA methylation inhibits transcription indirectly via a methyl-CpG binding protein. *Cell.* 64:1123–1134.
21. Nan, X., H. H. Ng, …, A. Bird. 1998. Transcriptional repression by the methyl-CpG-binding protein MeCP2 involves a histone deacetylase complex. *Nature.* 393:386–389.
22. Jones, P. L., G. J. Veenstra, …, A. P. Wolffe. 1998. Methylated DNA and MeCP2 recruit histone deacetylase to repress transcription. *Nat. Genet.* 19:187–191.
23. Ballestar, E., and A. P. Wolffe. 2001. Methyl-CpG-binding proteins. Targeting specific gene repression. *Eur. J. Biochem.* 268:1–6.

24. Straussman, R., D. Nejman, …, H. Cedar. 2009. Developmental programming of CpG island methylation profiles in the human genome. *Nat. Struct. Mol. Biol.* 16:564–571.

25. Lee, J. Y., and T. H. Lee. 2012. Effects of DNA methylation on the structure of nucleosomes. *J. Am. Chem. Soc.* 134:173–175.

26. Pérez, A., C. L. Castellazzi, …, M. Orozco. 2012. Impact of methylation on the physical properties of DNA. *Biophys. J.* 102:2140–2148.

27. Jimenez-Useche, I., J. Ke, …, C. Yuan. 2013. DNA methylation regulated nucleosome dynamics. *Sci. Rep.* 3:2121.

28. Collings, C. K., P. J. Waddell, and J. N. Anderson. 2013. Effects of DNA methylation on nucleosome stability. *Nucleic Acids Res.* 41:2918–2931.

29. Jimenez-Useche, I., D. Shim, …, C. Yuan. 2014. Unmethylated and methylated CpG dinucleotides distinctively regulate the physical properties of DNA. *Biopolymers.* 101:517–524.

30. Lee, J. Y., J. Lee, …, T. H. Lee. 2015. Dynamics of nucleosome assembly and effects of DNA methylation. *J. Biol. Chem.* 290:4291–4303.

31. Ngo, T. T., J. Yoo, …, T. Ha. 2016. Effects of cytosine modifications on DNA flexibility and nucleosome mechanical stability. *Nat. Commun.* 7:10813.

32. Langecker, M., A. Ivankin, …, M. Wanunu. 2015. Nanopores suggest a negligible influence of CpG methylation on nucleosome packaging and stability. *Nano Lett.* 15:783–790.

33. Dantas Machado, A. C., T. Zhou, …, R. Rohs. 2015. Evolving insights on how cytosine methylation affects protein-DNA binding. *Brief. Funct. Genomics.* 14:61–73.

34. Kalodimos, C. G., N. Biris, …, R. Kaptein. 2004. Structure and flexibility adaptation in nonspecific and specific protein-DNA complexes. *Science.* 305:386–389.

35. Boehr, D. D., R. Nussinov, and P. E. Wright. 2009. The role of dynamic conformational ensembles in biomolecular recognition. *Nat. Chem. Biol.* 5:789–796.

36. Rohs, R., X. Jin, …, R. S. Mann. 2010. Origins of specificity in protein-DNA recognition. *Annu. Rev. Biochem.* 79:233–269.

37. van der Vaart, A. 2015. Coupled binding-bending-folding: the complex conformational dynamics of protein-DNA binding studied by atomistic molecular dynamics simulations. *Biochim. Biophys. Acta.* 1850:1091–1098.

38. Ngo, T. T., Q. Zhang, …, T. Ha. 2015. Asymmetric unwrapping of nucleosomes under tension directed by DNA local flexibility. *Cell.* 160:1135–1144.

39. Geahigan, K. B., G. A. Meints, …, G. P. Drobny. 2000. The dynamic impact of CpG methylation in DNA. *Biochemistry.* 39:4939–4946.

40. Derreumaux, S., M. Chaoui, …, S. Fermandjian. 2001. Impact of CpG methylation on structure, dynamics and solvation of cAMP DNA responsive element. *Nucleic Acids Res.* 29:2314–2326.

41. Severin, P. M., X. Zou, …, K. Schulten. 2011. Cytosine methylation alters DNA mechanical properties. *Nucleic Acids Res.* 39:8740–8751.

42. Lankaš, F., J. Šponer, …, J. Langowski. 2000. Sequence-dependent elastic properties of DNA. *J. Mol. Biol.* 299:695–709.

43. Lavery, R., K. Zakrzewska, …, J. Sponer. 2010. A systematic molecular dynamics study of nearest-neighbor effects on base pair and base pair step conformations and fluctuations in B-DNA. *Nucleic Acids Res.* 38:299–313.

44. Karolak, A., and A. van der Vaart. 2014. Enhanced sampling simulations of DNA step parameters. *J. Comput. Chem.* 35:2297–2304.

45. Pasi, M., J. H. Maddocks, …, R. Lavery. 2014. μABC: a systematic microsecond molecular dynamics study of tetranucleotide sequence effects in B-DNA. *Nucleic Acids Res.* 42:12272–12283.

46. Teng, X., and W. Hwang. 2016. Elastic energy partitioning in DNA deformation and binding to proteins. *ACS Nano.* 10:170–180.

47. Ma, N., and A. van der Vaart. 2016. Anisotropy of B-DNA groove bending. *J. Am. Chem. Soc.* 138:9951–9958.

48. Nathan, D., and D. M. Crothers. 2002. Bending and flexibility of methylated and unmethylated EcoRI DNA. *J. Mol. Biol.* 316:7–17.

49. Temiz, N. A., D. E. Donohue, …, J. R. Collins. 2012. The role of methylation in the intrinsic dynamics of B- and Z-DNA. *PLoS One.* 7:e35558.

50. Carvalho, A. T., L. Gouveia, …, S. C. Kamerlin. 2014. Understanding the structural and dynamic consequences of DNA epigenetic modifications: computational insights into cytosine methylation and hydroxymethylation. *Epigenetics.* 9:1604–1612.

51. Renciuk, D., O. Blacque, …, B. Spingler. 2013. Crystal structures of B-DNA dodecamer containing the epigenetic modifications 5-hydroxymethylcytosine or 5-methylcytosine. *Nucleic Acids Res.* 41:9891–9900.

52. Wanunu, M., D. Cohen-Karni, …, M. Drndic. 2011. Discrimination of methylcytosine from hydroxymethylcytosine in DNA molecules. *J. Am. Chem. Soc.* 133:486–492.

53. Fenimore, P. W., H. Frauenfelder, …, F. G. Parak. 2002. Slaving: solvent fluctuations dominate protein dynamics and functions. *Proc. Natl. Acad. Sci. USA.* 99:16047–16051.

54. Bellissent-Funel, M. C., A. Hassanali, …, A. E. Garcia. 2016. Water determines the structure and dynamics of proteins. *Chem. Rev.* 116:7673–7697.

55. Duboué-Dijon, E., A. C. Fogarty, …, D. Laage. 2016. Dynamical disorder in the DNA hydration shell. *J. Am. Chem. Soc.* 138:7610–7620.

56. Laage, D., T. Elsaesser, and J. T. Hynes. 2017. Water dynamics in the hydration shells of biomolecules. *Chem. Rev.* 117:10694–10725.

57. Hsieh, C. L. 1997. Stability of patch methylation and its impact in regions of transcriptional initiation and elongation. *Mol. Cell. Biol.* 17:5897–5904.

58. Li, S., and C. E. Mason. 2014. The pivotal regulatory landscape of RNA modifications. *Annu. Rev. Genomics Hum. Genet.* 15:127–150.

59. Leijon, M., and A. Gräslund. 1992. Effects of sequence and length on imino proton exchange and base pair opening kinetics in DNA oligonucleotide duplexes. *Nucleic Acids Res.* 20:5339–5343.

60. Noy, A., A. Pérez, …, M. Orozco. 2007. Theoretical study of large conformational transitions in DNA: the B<–>A conformational change in water and ethanol/water. *Nucleic Acids Res.* 35:3330–3338.

61. Zgarbová, M., M. Otyepka, …, P. Jurečka. 2014. Base pair fraying in molecular dynamics simulations of DNA and RNA. *J. Chem. Theory Comput.* 10:3177–3189.

62. Lu, X. J., and W. K. Olson. 2008. 3DNA: a versatile, integrated software system for the analysis, rebuilding and visualization of three-dimensional nucleic-acid structures. *Nat. Protoc.* 3:1213–1227.

63. Brooks, B. R., C. L. Brooks, III, …, M. Karplus. 2009. CHARMM: the biomolecular simulation program. *J. Comput. Chem.* 30:1545–1614.

64. Foloppe, N., and A. D. MacKerell, Jr. 1999. Intrinsic conformational properties of deoxyribonucleosides: implicated role for cytosine in the equilibrium among the A, B, and Z forms of DNA. *Biophys. J.* 76:3206–3218.

65. Hart, K., N. Foloppe, …, A. D. Mackerell, Jr. 2012. Optimization of the CHARMM additive force field for DNA: improved treatment of the BI/BII conformational equilibrium. *J. Chem. Theory Comput.* 8:348–362.

66. Jorgensen, W. L., J. Chandrasekhar, …, M. L. Klein. 1983. Comparison of simple potential functions for simulating liquid water. *J. Chem. Phys.* 79:926–935.

67. Noy, A., and R. Golestanian. 2012. Length scale dependence of DNA mechanical properties. *Phys. Rev. Lett.* 109:228101.

68. Pérez, A., F. J. Luque, and M. Orozco. 2012. Frontiers in molecular dynamics simulations of DNA. *Acc. Chem. Res.* 45:196–205.

69. Feller, S. E., Y. Zhang, …, B. R. Brooks. 1995. Constant pressure molecular dynamics simulation: the Langevin piston method. *J. Chem. Phys.* 103:4613–4621.

70. Ryckaert, J.-P., G. Ciccotti, and H. J. C. Berendsen. 1977. Numerical integration of the cartesian equations of motion of a system with constraints: molecular dynamics of n-alkanes. *J. Comput. Phys.* 23:327–341.

71. Feller, S. E., R. W. Pastor, …, B. R. Brooks. 1996. Effect of electrostatic force truncation on interfacial and transport properties of water. *J. Phys. Chem.* 100:17011–17020.

72. Hynninen, A. P., and M. F. Crowley. 2014. New faster CHARMM molecular dynamics engine. *J. Comput. Chem.* 35:406–413.

73. Humphrey, W., A. Dalke, and K. Schulten. 1996. VMD: visual molecular dynamics. *J. Mol. Graph.* 14:33–38, 27–28.

74. Pettersen, E. F., T. D. Goddard, …, T. E. Ferrin. 2004. UCSF Chimera–a visualization system for exploratory research and analysis. *J. Comput. Chem.* 25:1605–1612.

75. Reif, F. 1965. Fundamentals of Statistical and Thermal Physics. McGraw-Hill, New York.

76. Ravikumar, K. M., and W. Hwang. 2011. Role of hydration force in the self-assembly of collagens and amyloid steric zipper filaments. *J. Am. Chem. Soc.* 133:11766–11773.

77. Goriely, A., and M. Tabor. 1997. Nonlinear dynamics of filaments I. Dynamical instabilities. *Physica D.* 105:20–44.

78. Falk, M., K. A. Hartman, and R. Lord. 1962. Hydration of deoxyribonucleic acid. I. A gravimetric study. *J. Am. Chem. Soc.* 84:3843–3846.

79. Floisand, D. J., and S. A. Corcelli. 2015. Computational study of phosphate vibrations as reporters of DNA hydration. *J. Phys. Chem. Lett.* 6:4012–4017.

80. Siebert, T., B. Guchhait, …, T. Elsaesser. 2016. Range, magnitude, and ultrafast dynamics of electric fields at the hydrated DNA surface. *J. Phys. Chem. Lett.* 7:3131–3136.

81. Blokzijl, W., and J. B. F. N. Engberts. 1993. Hydrophobic effects. Opinions and facts. *Angew. Chem. Int. Ed.* 32:1545–1579.

82. Feig, M., and B. M. Pettitt. 1998. Crystallographic water sites from a theoretical perspective. *Structure.* 6:1351–1354.

83. Arai, S., T. Chatake, …, N. Niimura. 2005. Complicated water orientations in the minor groove of the B-DNA decamer d(CCATTAATGG)2 observed by neutron diffraction measurements. *Nucleic Acids Res.* 33:3017–3024.

84. Feig, M., and B. M. Pettitt. 1999. Sodium and chlorine ions as part of the DNA solvation shell. *Biophys. J.* 77:1769–1781.

85. Makarov, V., B. M. Pettitt, and M. Feig. 2002. Solvation and hydration of proteins and nucleic acids: a theoretical view of simulation and experiment. *Acc. Chem. Res.* 35:376–384.

86. Galindo-Murillo, R., J. C. Robertson, …, T. E. Cheatham, III. 2016. Assessing the current state of Amber force field modifications for DNA. *J. Chem. Theory Comput.* 12:4114–4127.

87. Savelyev, A., and A. D. MacKerell, Jr. 2014. All-atom polarizable force field for DNA based on the classical Drude oscillator model. *J. Comput. Chem.* 35:1219–1239.

88. Lemkul, J. A., and A. D. MacKerell, Jr. 2017. Polarizable force field for DNA based on the classical Drude oscillator: II. Microsecond molecular dynamics simulations of duplex DNA. *J. Chem. Theory Comput.* 13:2072–2085.

89. Vafabakhsh, R., and T. Ha. 2012. Extreme bendability of DNA less than 100 base pairs long revealed by single-molecule cyclization. *Science.* 337:1097–1101.

90. Le, T. T., and H. D. Kim. 2013. Measuring shape-dependent looping probability of DNA. *Biophys. J.* 104:2068–2076.

91. Le, T. T., and H. D. Kim. 2014. Probing the elastic limit of DNA bending. *Nucleic Acids Res.* 42:10786–10794.

92. Salari, H., B. Eslami-Mossallam, …, M. R. Ejtehadi. 2015. Extreme bendability of DNA double helix due to bending asymmetry. *J. Chem. Phys.* 143:104904.

Biophysical Journal, Volume *114*

Supplemental Information

Effect of Methylation on Local Mechanics and Hydration Structure of DNA

Xiaojing Teng and Wonmuk Hwang

SUPPORTING MATERIAL

Effect of methylation on local mechanics and hydration structure of DNA

Xiaojing Teng[†,§], Wonmuk Hwang[*,†,‡,¶]
[†]Department of Biomedical Engineering, [‡]Department of Materials Science & Engineering,
Texas A&M University, College Station, Texas 77843, USA
[¶]School of Computational Sciences, Korea Institute for Advanced Study, Seoul 02455, Korea
[§]Current address: Department of Chemistry, Georgetown University, Washington D.C. 20057, USA
[*]To whom correspondence should be addressed. Email: hwm@tamu.edu

Step [oligo]	s (Å)	$\boldsymbol{p_M}$	$\boldsymbol{p_m}$	θ_t	$\sigma(s)$	$\sigma(\theta_M)$	$\sigma(\theta_m)$
cg/cg [AAAcg]	3.3760	(-0.2946,0.9556,0.0001)	(0.9524,0.2936,-0.0825)	22.28±4.75	0.40	6.10	3.47
CG/CG [AAACG]	3.3746	(-0.3033,0.9529,-0.0082)	(0.9501,0.3017,-0.0796)	21.11±5.06	0.44	6.31	3.38
cg/cg [TTTcg]	3.7837	(-0.2350,0.9720,-0.0005)	(0.9685,0.2341,-0.0853)	18.49±6.34	0.40	6.11	3.30
CG/CG [TTTCG]	3.8043	(-0.2457,0.9694,0.0033)	(0.9661,0.2451,-0.0812)	16.20±6.33	0.41	6.54	3.19
cg/cg $[cg]_8$	3.3268	(-0.3032,0.9529,-0.0028)	(0.9467,0.3009,-0.1150)	21.43±4.83	0.37	5.70	3.61
cg/cg [CGcg]	3.4435	(-0.3276,0.9448,0.0028)	(0.9410,0.3265,-0.0893)	19.22±5.39	0.37	5.82	3.15
Ac/gT [AAAcg]	3.6184	(-0.1878,0.9821,0.0157)	(0.9767,0.1885,-0.1023)	19.44±4.50	0.32	6.22	2.42
AC/GT [AAACG]	3.6432	(-0.2179,0.9759,0.0139)	(0.9698,0.2181,-0.1088)	18.15±5.24	0.35	6.91	2.80
gA/Tc [TTTcg]	3.7112	(-0.4580,0.8889,-0.0103)	(0.8885,0.4574,-0.0369)	6.04±5.18	0.35	5.46	2.86
GA/TC [TTTCG]	3.6877	(-0.4465,0.8948,0.0001)	(0.8944,0.4463,-0.0298)	8.18±6.18	0.40	5.91	3.42
gc/gc $[cg]_8$	3.5599	(-0.2572,0.9664,-0.0009)	(0.9630,0.2563,-0.0830)	14.52±5.33	0.28	4.92	2.18
Gc/gC [CGcg]	3.5245	(-0.2145,0.9767,0.0076)	(0.9727,0.2143,-0.0891)	17.82±6.26	0.30	5.29	2.39

Table S1: Equilibrium conformations of dinucleotide steps analyzed in this study. The first column shows the name of a step and the oligo from which calculations were made (sequences of oligos are in Table 1). Names with all capital letters are for non-methylated oligos. s: Average distance between centroids; $\boldsymbol{p_M}$ and $\boldsymbol{p_m}$: Coordinates of the major and minor principal axes relative to the triad of the reference base pair. These set $\boldsymbol{p_t} = \boldsymbol{p_m} \times \boldsymbol{p_M}$. θ_t: Average and standard deviation of the twist angle (degrees). $\sigma(s)$, $\sigma(\theta_M)$, and $\sigma(\theta_m)$: Standard deviations of the distance between centroids (Å), and the major and the minor bending angles (degrees), respectively.

Step [oligo]	κ_M ($\times 10^4$)	κ_m ($\times 10^4$)	κ_t ($\times 10^4$)	κ_E
cg/cg [AAAcg]	1.23 (1.15)	3.82 (4.02)	2.04 (1.79)	262 (218)
cg/cg [TTTcg]	1.38 (1.21)	4.73 (5.08)	1.28 (1.29)	254 (241)
cg/cg $[cg]_8$	1.39 (1.24)	3.48 (3.95)	1.94 (1.66)	305 (308)
cg/cg [CGcg]	1.29 (1.24)	3.76 (3.95)	1.61 (1.66)	301 (308)
Ac/gT [AAAcg]	1.27 (1.04)	8.40 (6.30)	2.43 (1.81)	416 (344)
gA/Tc [TTTcg]	1.69 (1.44)	6.15 (4.28)	1.88 (1.31)	338 (256)
gc/gc $[cg]_8$	2.00 (1.47)	10.14 (5.84)	1.70 (1.02)	521 (384)
Gc/gC [CGcg]	1.71 (1.47)	8.38 (5.84)	1.22 (1.02)	450 (384)

Table S2: Average stiffness of steps in methylated oligos (*cf.*, Fig. 3). κ_M (major bending), κ_m (minor bending), and κ_t (twist) are in pN·Å^2, and κ_E (extension) is in pN/Å. Reference values from non-methylated oligos are in parentheses. In case an oligo contains multiple steps of the same type (such as cg/cg in $[cg]_8$), the corresponding stiffness were averaged over those steps.

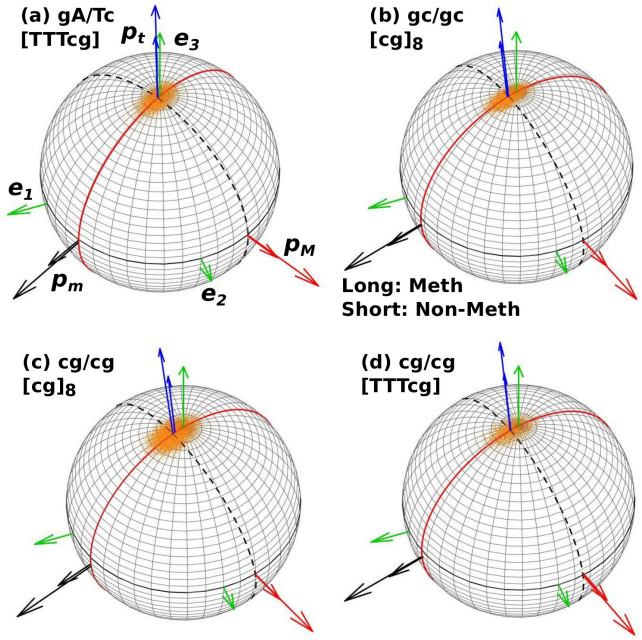

Figure S1: Principal axis-based analysis. (a) gA/Tc step in [TTTcg], (b) gc/gc step in $[cg]_8$, (c) cg/cg step in $[cg]_8$, and (d) cg/cg step in [TTTcg]. See Fig. 1 for explanation.

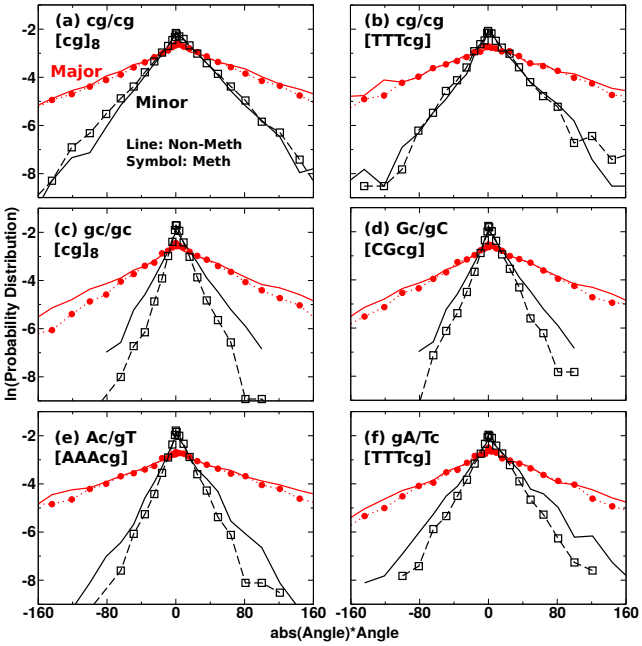

Figure S2: Distributions of major and minor bending angles plotted on logarithmic scale (*cf.*, Fig. 2). For the horizontal axis, sign(Angle)$\times$(Angle)^2 is used. In this way, a Gaussian distribution appears as two straight lines.

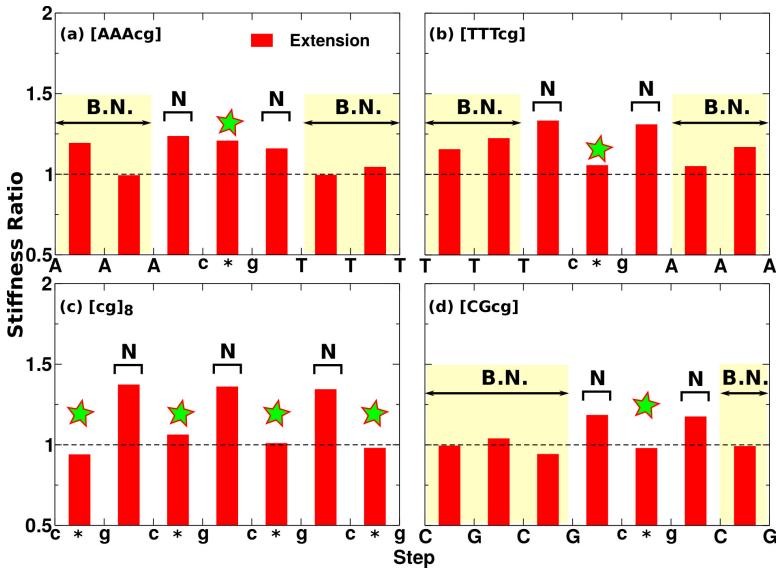

Figure S3: Ratio of extensional stiffness between methylated and non-methylated oligos. Symbols are explained in Fig. 3. Similar to the bending and twist stiffness, the ratio increases for steps neighboring the ^{Me}CpG step.

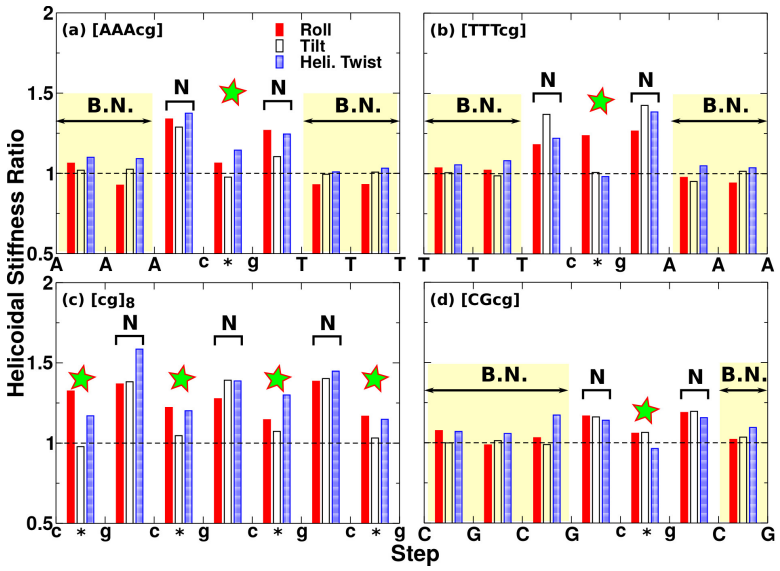

Figure S4: Ratio between the apparent stiffness of roll, tilt, and helicoidal twist for dinucleotide steps between methylated and non-methylated oligos. The same simulations for Fig. 3 were used for analysis. Note that the vertical axis has the same range as in Fig. 3, which illustrates that the principal axis-based analysis reveals stiffness changes more clearly.

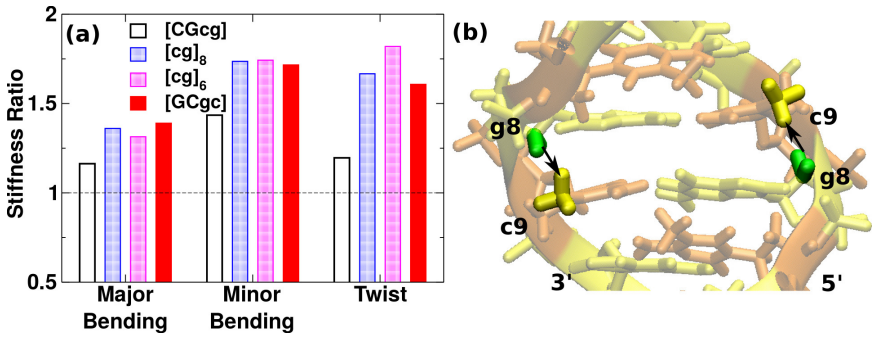

Figure S5: Origin of the stiffness enhancement in consecutively methylated CG-repeats. (a) Stiffness ratios of the gc/gc step in [CGcg], $[cg]_8$, $[cg]_6$, and [GCgc], relative to the non-methylated GC/GC step (*cf.*, Fig. 3). Although [GCgc] has only a single $Gp^{Me}C$ step, its stiffness enhancement is comparable to those of $[cg]_6$ and $[cg]_8$. (b) Illustration of the dual interactions between mCYT-methyl and and the neighboring C2'-methylene groups in the $Gp^{Me}C$ step.

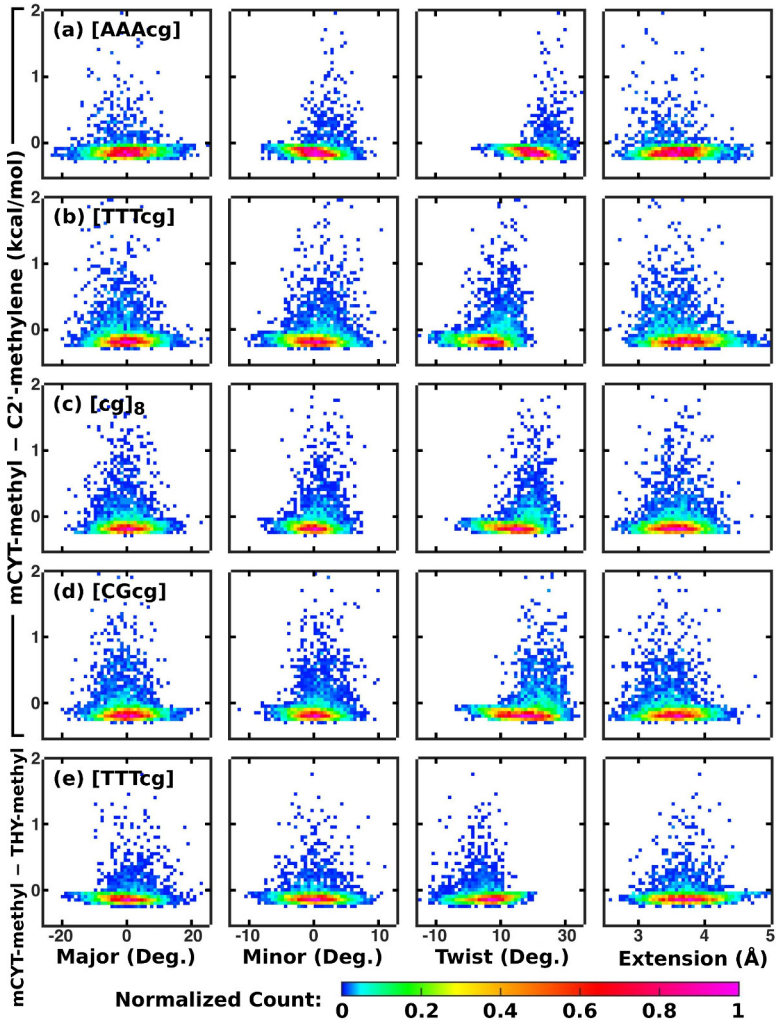

Figure S6: 2D-histograms of order parameters vs. the interaction energy (electrostatic and Lennard-Jones) between the mCYT-methyl group with (a–d) the neighboring C2'-methylene and (e) the THY-methyl group in [TTTcg] on the 5'-side. The skewing directions of histograms are opposite to those for the minimum distance histograms (Fig. 5).

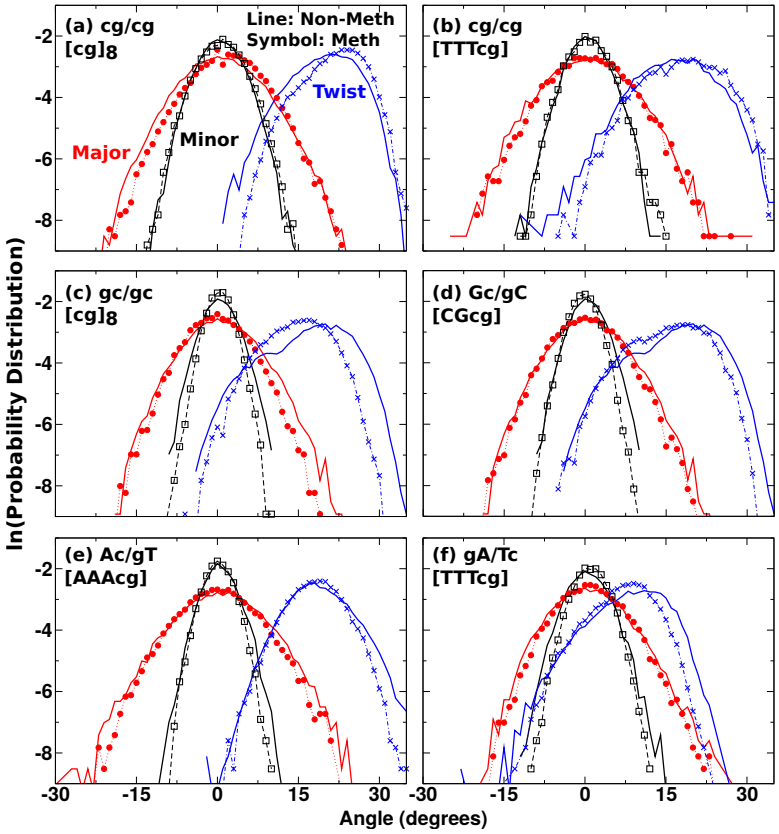

Figure S7: Distributions of angles based on the equilibrium triads of non-methylated oligos. Distributions for the non-methylated oligos are the same as those in Fig. 2, except that they are in logarithmic scale. For steps neighboring ^{Me}CpG (symbols in panels c–f), larger angles tend to be suppressed more compared to smaller angles, which is consistent with the mechanism illustrated in Fig. 4.

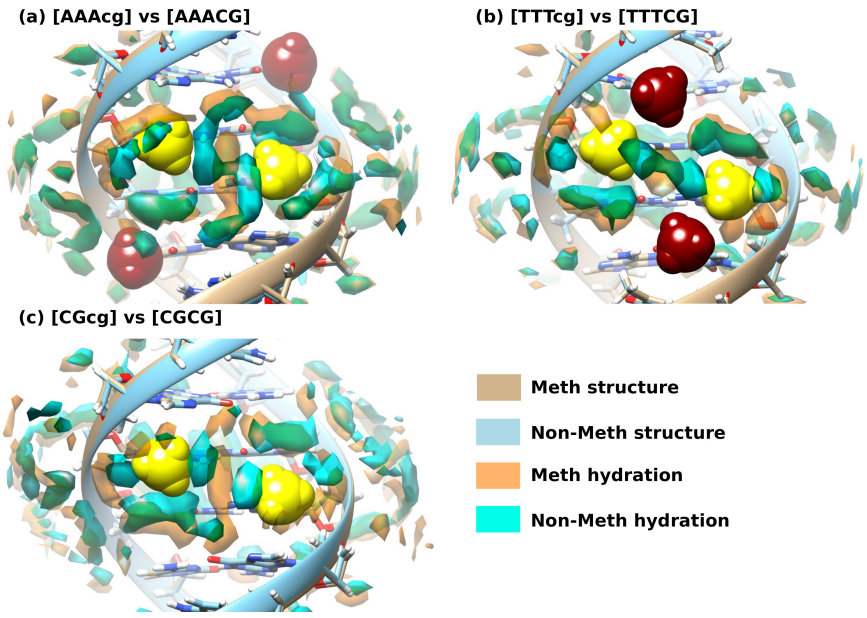

Figure S8: Overlaid hydration maps around the ^{Me}CpG (orange) and the corresponding non-methylated CG/CG (cyan) steps (*c*f., Fig. 6). Due to their transparency, overlapping regions of density maps appear in darker green colors.

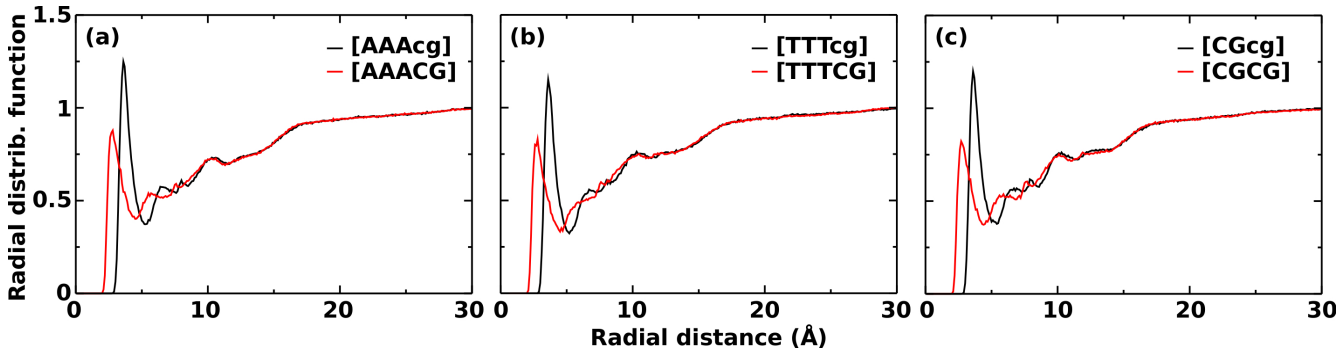

Figure S9: Radial distribution function of water oxygen around the carbon atom in the mCYT-methyl group (black) and the H5 atom in the corresponding position of the non-methylated CYT (red). Distributions are normalized by the bulk water density ($\sim$0.033313/Å^3).

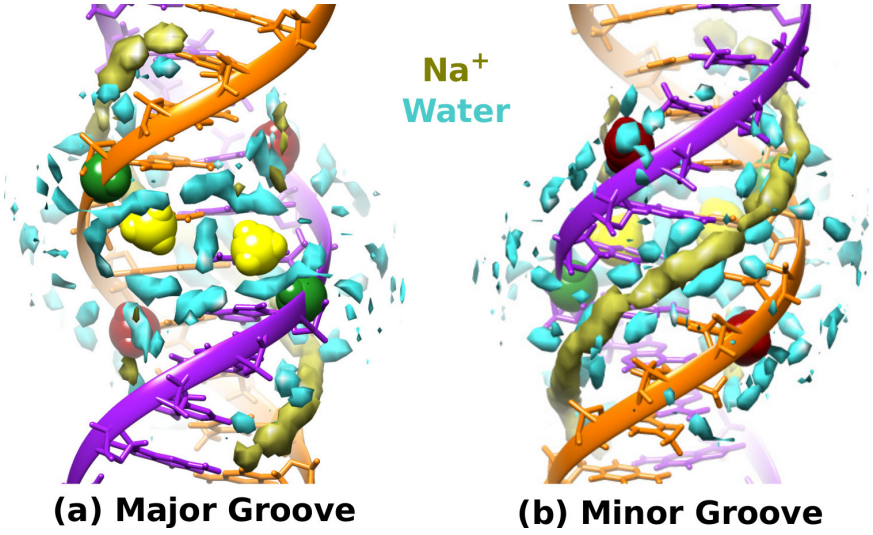

Figure S10: Density of sodium ions (khaki). [AAAcg] is used as an example. Water density is colored uniformly in cyan. Density cutoffs used are, in multiples of the bulk water density: 0.2 times for for Na^+, and 2 times for water.

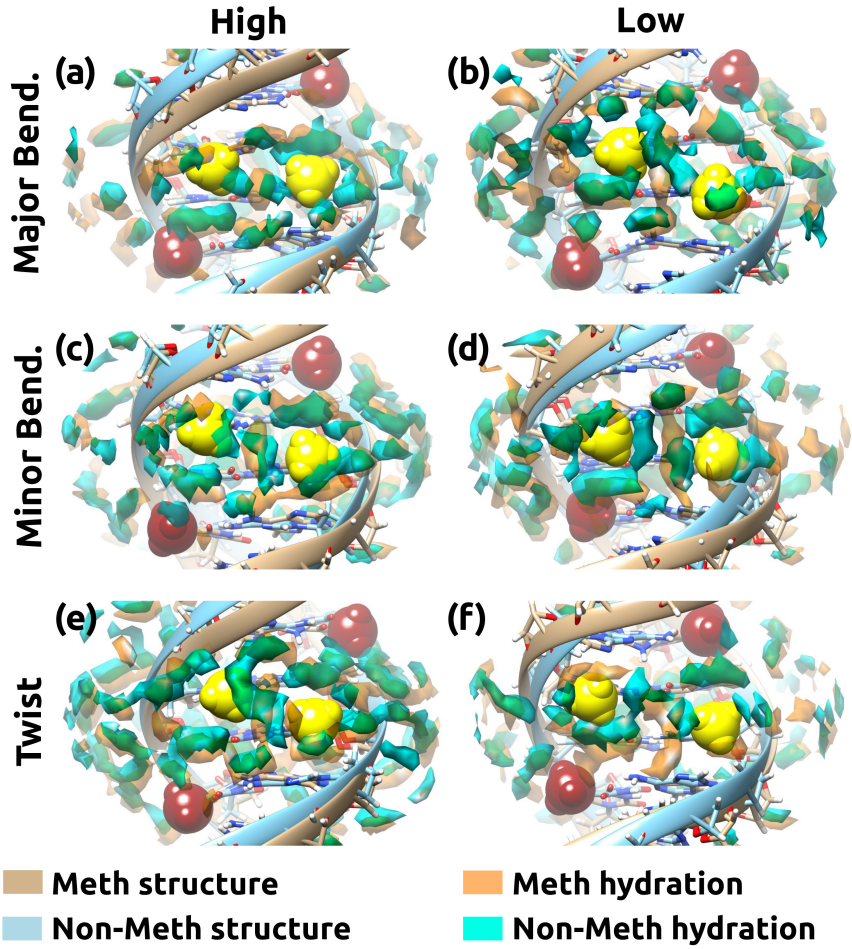

Figure S11: Overlaid hydration maps around the ^{Me}CpG (orange; [AAAcg]) and the corresponding non-methylated CG/CG (cyan; [AAACG]) steps under high deformations (*cf.*, Fig. 7). Due to their transparency, overlapping regions of density maps appear in darker green colors. Since deformed structures are used as reference, they do not align as well compared those in Fig. S8. Alignments are worse for the neighboring steps whose stiffness between methylated and non-methylated cases differ. For this reason, overlaid maps corresponding to Fig. 8 were not generated.